Correspondence to:
C. Schmidt,
cschmidt@geomar.de

Origin of High Mg and SO4 Fluids in Sediments of the Terceira Rift, Azores-Indications for Caminite Dissolution in a Waning Hydrothermal System

C. Schmidt[1] (iD), C. Hensen[1] (iD), K. Wallmann[1], V. Liebetrau[1], M. Tatzel[2,3], S. L. Schurr[4], S. Kutterolf[1] (iD), L. Haffert[1], S. Geilert[1] (iD), C. Hübscher[5] (iD), E. Lebas[6] (iD), A. Heuser[1] (iD), M. Schmidt[1] (iD), H. Strauss[4] (iD), J. Vogl[2] (iD), and T. Hansteen[1] (iD)

[1]GEOMAR Helmholtz Centre for Ocean Research Kiel, Kiel, Germany, [2]Bundesanstalt für Materialforschung und -prüfung, Berlin, Germany, [3]Department of Earth and Planetary Sciences, University of California, Santa Cruz, CA, USA, [4]Institut für Geologie und Paläontologie, Westfälische Wilhelms-Universität Münster, Münster, Germany, [5]Institute of Geophysics, University of Hamburg, Hamburg, Germany, [6]Institute of Geophysics, University of Kiel, Kiel, Germany

Abstract During R/V *Meteor* cruise 141/1, pore fluids of near surface sediments were investigated to find indications for hydrothermal activity in the Terceira Rift (TR), a hyperslow spreading center in the Central North Atlantic Ocean. To date, submarine hydrothermal fluid venting in the TR has only been reported for the D. João de Castro seamount, which presently seems to be inactive. Pore fluids sampled close to a volcanic cone at 2,800-m water depth show an anomalous composition with Mg, SO4, and total alkalinity concentrations significantly higher than seawater and a nearby reference core. The most straightforward way of interpreting these deviations is the dissolution of the hydrothermally formed mineral caminite ($MgSO_4$ 0.25 Mg $(OH)_2$ 0.2H_2O). This interpretation is corroborated by a thorough investigation of fluid isotope systems ($\delta^{26}Mg$, $\delta^{30}Si$, $\delta^{34}S$, $\delta^{44/42}Ca$, and $^{87}Sr/^{86}Sr$). Caminite is known from mineral assemblages with anhydrite and forms in hydrothermal recharge zones only under specific conditions such as high fluid temperatures and in altered oceanic crust, which are conditions generally met at the TR. We hypothesize that caminite was formed during hydrothermal activity and is now dissolving during the waning state of the hydrothermal system, so that caminite mineralization is shifted out of its stability zone. Ongoing fluid circulation through the basement is transporting the geochemical signal via slow advection toward the seafloor.

Plain Language Summary Hydrothermal vents are a common phenomenon in oceanic spreading centers worldwide. During Meteor cruise 141/1 we sampled sediments and extracted pore fluids to find the first indications for hydrothermal activity in the Terceira Rift. The results indicate that a hydrothermal vent close to a major volcanic cone formed in the past and seems to be in a waning state at present. Sampled fluids are enriched in total alkalinity, Mg and SO4. We found that the most straightforward explanation for this unusual finding is the dissolution of the hydrothermally formed mineral caminite, a magnesium-sulfate-hydroxide-hydrate. Caminite is a rare mineral but suggested to be abundant under specific conditions in hydrothermal recharge zones. We propose that caminite formed in the Terceira Rift is now dissolving as temperatures decline, and fluids enriched in Mg and SO4 are transported along deep-rooted faults to the seafloor.

1. Introduction

Hydrothermal vents are common phenomena in slow- to fast-spreading centers worldwide (Beaulieu et al., 2013). Numerous authors provide a wealth of data on mineral assemblages and fluid chemistry of hydrothermal systems and their recharge zones (e.g., Alt, 1995; Teagle et al., 1998). Hydrothermal fluid circulation is a driver for cooling of the Earth's crust and also plays a major role in geochemical fluxes (Elderfield & Schultz, 1996). Generally, high-temperature reactions are the reason that fluids become depleted in Mg and SO4 while Ca and fluid-mobile elements like Li are enriched. Mg is quantitatively removed from fluids by the formation of Mg-rich smectite such as saponite (Alt & Honnorez, 1984). SO4 in hydrothermal systems can undergo various reactions. At temperatures above 150 °C, SO4 is typically removed by the precipitation of anhydrite (Alt et al., 1986; Teagle et al., 1998). However, SO4 can also be reduced and precipitate as sulfide mineral (Alt, 1995). Ca is leached from the basement during albitization of plagioclase (Alt et al., 1986;
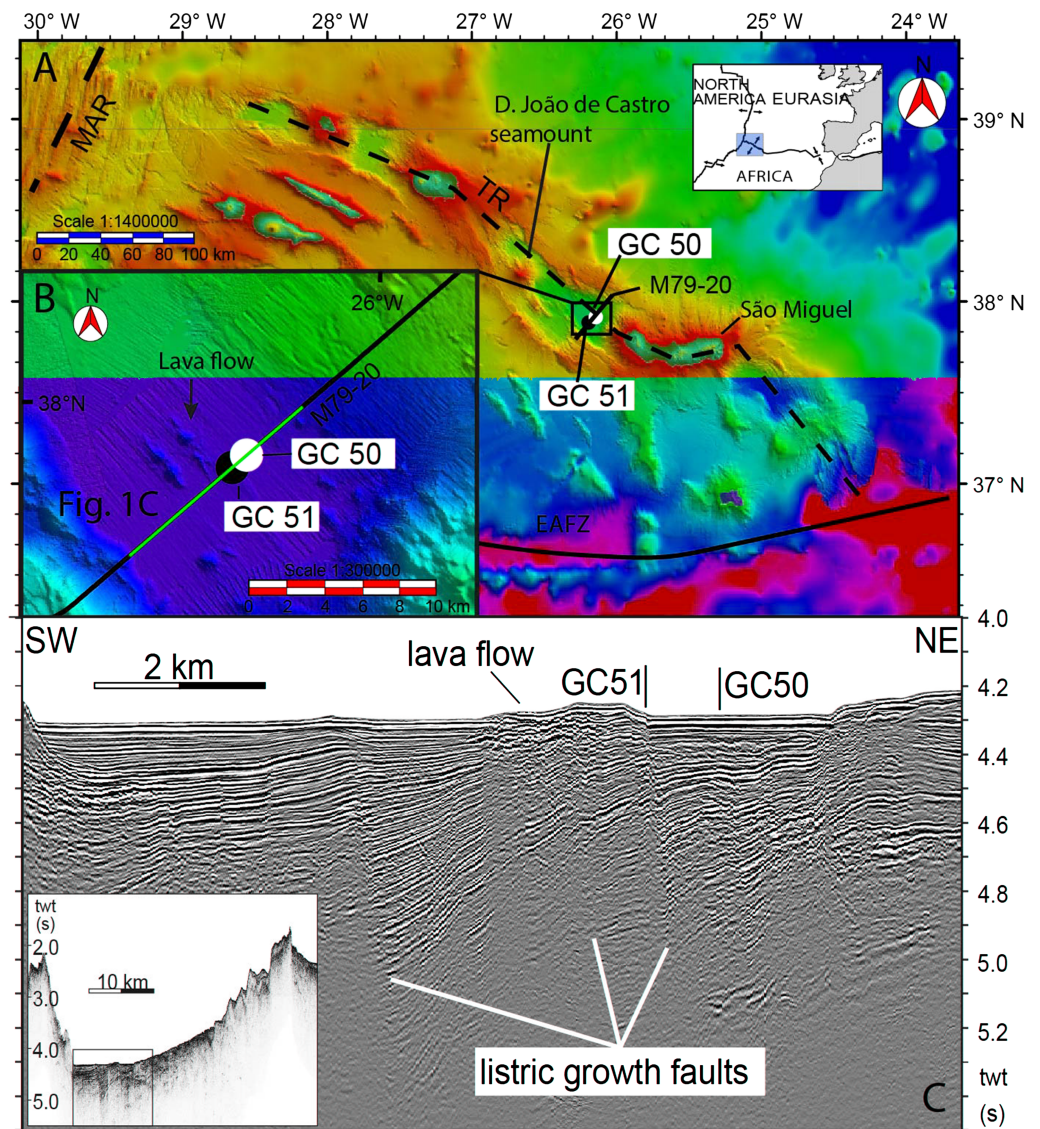
Figure 1. Overview Map: (a) Regional overview map modified from Weiß et al. (2015); TR: Terceira Rift; MAR: Mid-Atlantic Ridge; EAFZ: East Azores fracture zone; (b) detailed bathymetry map of core locations close to volcanic cone in the TR; (c) Multichannel seismic profile M79-20 crossing TR.

Humphris & Thompson, 1978). Levels of enrichment can vary, but concentrations of Ca in fluids can reach up to 80 mM (e.g., Butterfield et al., 1994). There are few studies focusing on mineral dissolution after cooling of hydrothermal fluid circulation (e.g., Gieskes et al., 2002; Gruen et al., 2014), leading to substantial changes in fluid compositions (e.g., enrichment in SO_4 and Ca due to anhydrite dissolutions, brine formation due to leaching of hydrothermally formed salts in the subsurface).

The Terceira Rift (TR) is a ~500-km WNW-ESE striking rift in the Central North Atlantic Ocean, marking the plate boundary between Nubia and Eurasia. The TR has been described as a hyperslow spreading center with a spreading rate of 4 mm a^{-1} (Vogt & Jung, 2004). Cutting through the Azores Plateau, the TR comprises four basins and passes through three volcanic islands of the Azores Archipelago (Figure 1). Albeit ongoing magmatic activity in this region, only nine onshore hydrothermal springs (Couto et al., 2015), and one offshore submarine vent, located at the D. João de Castro seamount (Figure 1), have been reported to date (Figure 1; Cardigos et al., 2005). However, during a previous Meteor expedition (M 128) in 2016 no signs of hydrothermal activity was detected at this location (Beier, 2016). Weiß et al. (2015) reported on 252 volcanic cones and sills in the eastern TR and the flanks of São Miguel, which possibly could host

hydrothermal systems. In the southern Hirondelle Basin major volcanic cones are connected to listric faults along the rift axis of the TR (Figure 1c), providing a potential pathway for the ascent of hydrothermal fluids to the seafloor. One of the major cones shows no sediment cover in the backscatter data (Weiß et al., 2015), which can be regarded as sign for recent magmatic activity. This volcanic cone provides presumably good preconditions to host a hydrothermal system. During R/V *Meteor* cruise M141/1 in September 2017 we sampled pore fluids by gravity coring in the vicinity of the elongated volcanic cone to detect potential signs of ongoing hydrothermal activity in the TR.

2. Materials and Methods

2.1. Pore Fluid and Sediment Sampling

Two gravity cores (GCs) were retrieved during the cruise at 2,800-m water depth. GC51 was taken on the fault close to the volcanic cone whereas GC50 was taken as a regional reference core (Figures 1b and 1c). Both GCs had a length of 5.75 m and were equipped with a plastic liner. Right after retrieval on deck, the plastic liner was cut into 1-m-long segments and head space samples for hydrocarbon gas analyses were taken. The sampling interval was between 5 and 20 cm. Sediment samples were squeezed in a cold room with an argon gas squeezer. On average, squeezing took about 10 min. Gas pressure was usually up to 5 bar. The pore fluid was filtered through 0.2-μm cellulose Whatmann filters.

2.2. Pore Fluid Analyses

On board analyses for total alkalinity (TA) were carried out using a METROHM titration unit 876 Dosimat plus. TA was determined by titration with 0.02 N HCl using a methyl red indicator. The solution was bubbled with argon to remove CO_2 gas released during the titration. On board analyses for NH_4 were carried out using a Hitachi U2800A spectrophotometer applying a calibration curve with eight standards covering the concentration range between 0 and 332.62 μM. In our shore-based laboratories at GEOMAR Helmholtz Center for Ocean Research, Kiel, cation concentrations (B, Ba, Ca, K, Li, Mg, Na, Si, and Sr) were determined using the Inductively Coupled Plasma Optical Emission Spectrometry (ICP-OES, JY 170 Ultrace, Jobin Yvon). Anion concentrations (Cl, Br, and SO_4) were analyzed using the Ion Chromatography (761 IC-Compact, Methrom). The IAPSO seawater standard was used to check the reproducibility and accuracy of the ICP-OES and IC chemical analyses (supplemental data; Gieskes et al., 1991). The reproducibility is in general better than 1% relative standard deviation (RSD) for each element. Detailed description of the methods can be found in for example, Hensen et al. (2007) and Scholz et al. (2009).

2.3. Solid Phase Analyses

Sediment samples from both cores were taken to determine their porosity, water content, chemical bulk analyses, and petrological description (see Tables S3 and S4 in the supporting information). For the chemical bulk analyses, sediments were dried at 65 °C for 24 hr and homogenized. One hundred milligrams of each sample was filled into a Savillex vessel and treated with 2 cm³ HF, 2 cm³ HNO_3, and 3 cm³ $HClO_4$ at 185 °C for 8 hr. Another 1 cm³ of HNO_3 was added to smoke off the acid. The full method description is available in Scholz et al. (2016). After treatment with acids, sediment samples were measured by inductively coupled plasma optical emission spectroscopy (ICP-OES) at GEOMAR, for concentrations of Al, Ca, Fe, K, Mg, Na, and Sr. The reproducibility is better than 1% RSD.

2.4. Smear Slides

Modal compositional data were obtained by counting at least 400 points in each of the 13 selected smear slides with a modified Gazzi-Dickinson method based on Decker and Helmold (1985) and von Eynatten and Gaupp (1999) using a microstep point-counting system and the Petroglide software without distinguishing into grain size fractions. The amount of 400 points was selected to derive a statistically significant estimation (e.g., Van der Plas & Tobi, 1965) of respective volume percentages of the components in the sediments. We distinguish between 13 juvenile and nonjuvenile components. On the basis of common features four characteristic groups (total glass, total lithics, microfossils, and clay) were defined. Volume percentages of components or modal groups given in the text are normalized to 100%. Percentage raw data and calculated volume percentages of modal groups are listed in Tables S6 and S7 in the supporting information. Minerals like pyroxene, feldspar, amphibole, different types of pyroclasts, and sedimentary and volcanic lithics have not been subdivided in different species. Biogenic material has been subdivided into the main components

Table 1
Pore Fluid Data GC50

Depth (cm)	NH4 (μM)	TA (meq/L)	B (mM)	Ca (mM)	Na (mM)	Mg (mM)	Sr (μM)	Si (mM)	Li (μM)	K (mM)	Cl (mM)	SO4 (mM)	Porosity (−)
12	11.40	2.99	0.464	10.68	483	53.8	87.2	0.19	28.1	10.7	559.7	28.6	
23	39.85	3.06	0.458	10.88	484	54.4	88.7	0.21	27.2	10.7	566.8	29.3	0.65
48	89.19	3.27	0.465	10.63	487	54.8	88.1	0.25	27.2	10.8	572.8	29.4	0.62
60	113.00	3.20	0.440	10.08	481	53.3	85.7	0.25	24.9	10.7	566.9	28.4	
71	123.80	3.20	0.445	9.81	480	52. 8	85.7	0.25	25.0	10.7	568.7	28.5	
85	159.90	3.58	0.467	10.29	487	54.7	88.7	0.23	26.3	10.8	574.9	29.2	0.62
108	186.30	3.71	0.476	10.02	486	54.7	88.1	0.22	25.7	10.6	572.5	28.6	0.82
118	188.10	3.63	0.455	9.72	483	53.6	85.9	0.21	24.1	10.2	569.1	28.4	
133	194.10	3.84	0.487	9.82	484	54.4	86.7	0.22	25.1	10.5	572.8	28.7	0.64

Note. Core Location: 37°58.345′N; 26°5.046′W; gray areas indicate ash and tephra layers.

(nannofossils and foraminifers), and minor abundances have been summarized in "biogenic rest." The reproducibility (2 times counting) was tested for two different samples and is better than 4% RSD regarding the modal groups. A detailed description can be found in the supporting information.

2.5. Si Isotopes

Pore fluid samples were prepared for Si isotope measurements following the purification method of Georg et al. (2006). The samples were loaded onto 1-ml precleaned cation-exchange resin (Biorad AG50 W-X8) and eluted with 2-ml Milli-Q water. Si isotopes were measured on the NuPlasma high-resolution Multicollector-Inductively Coupled Plasma Mass Spectrometer (HR MC-ICPMS) in medium resolution mode using the Cetac Aridus II desolvator at GEOMAR. The Si concentration after sample purification equaled ~22 μM, yielding Si recoveries of ≥99% and a procedural blank below detection limit. The measurements were executed using the standard sample bracketing method to account for mass bias drifts of the instrument (Albarède et al., 2004). Si isotopes are given in the $\delta^{30}Si$ notation, which represents the deviation of the sample $^{30}Si/^{28}Si$ from that of the international Si standard NBS28. Long-term $\delta^{30}Si$ values of the reference materials Big Batch (−10.6 ± 0.2‰; 2 SD; $n = 49$), IRMM018 (−1.5 ± 0.2‰; $n = 48$), and Diatomite (+1.3 ± 0.2‰; 2 SD; $n = 44$) agree well with published $\delta^{30}Si$ values in the literature (e.g., Reynolds et al., 2007). Additionally, an in-house pore fluid matrix standard has been measured, which yielded an average $\delta^{30}Si$ value of +1.3 ± 0.2‰ (2 SD; $n = 17$). All samples were measured 2–3 times on different days and the resulting $\delta^{30}Si$ values have uncertainties between 0.1 and 0.2‰ (2 SD).

2.6. Sulfur Isotopes

Pore fluids were filtered (0.2-μm pore size filter) and acidified (25% HCl) to a pH below 2. Subsequently, $BaCl_2$ solution (8.5%) was added to precipitate barium sulfate at 80 °C. The $BaSO_4$ precipitate was obtained via filtration using a cellulose nitrate filter (0.45-μm pore size). For $\delta^{34}S$ measurement 0.4-mg barium sulfate mixed with 0.4- to 0.8-mg V_2O_5 (catalyst) was placed into tin capsules. The $\delta^{34}S$ values were determined using an EA-IRMS (Thermo Scientific Delta V advantage coupled with a Flash-EA-IsoLink-CN Elemental Analyzer) at the Institute of Geology, Westfälische Wilhelms-Universität of Münster, and are reported in the standard delta notation as per mil difference to the Vienna-Canyon Diablo Troilite (V-CDT) standards. Analytical performance was monitored using international reference materials IAEA S-1, S-2, S-3, and NBS 127 with an external reproducibility better than 0.6‰ (2 SD). For $\delta^{18}O_{SO4}$ analysis 0.2-mg barium sulfate was placed in a silver capsule, and $\delta^{18}O_{SO4}$ was determined with a TC/EA-IRMS (Thermo Scientific Delta V plus connected with a high-temperature pyrolysis unit). The $\delta^{18}O_{SO4}$ values are reported as per mil difference to the V-SMOW standard. Measurement of replicate samples and reference materials (IAEA-SO-5, IAEA -SO-6, and NBS 127) yielded an external reproducibility better than 1.0‰ (2 SD).

2.7. Sr Isotopes

Sr isotope ratios ($^{87}Sr/^{86}Sr$) were measured by thermal ionization mass spectrometry (TIMS, TRITON, ThermoFisher Scientific) at the GEOMAR on aliquots of the original ICP-OES pore water samples

Table 2
Pore Fluid Data GC51

Depth (cm)	NH4 (µM)	TA (meq/L)	B (mM)	Ca (mM)	Na (mM)	Mg (mM)	Sr (µM)	Si (mM)	Li (µM)	K (mM)	Cl (mM)	SO4 (mM)	Porosity (−)
16	64.57	4.05	0.448	10.66	485	55.7	101.8	0.21	29.5	10.3	560.6	29.5	0.59
30	88.09	4.67	0.452	10.41	481	55.5	109.6	0.22	28.9	9.8	564.7	29.4	
40	114.50	4.94	0.473	10.79	490	57.4	116.9	0.25	31.9	10.5	571.8	30.3	0.61
50	140.10	5.27	0.481	10.60	488	57.4	118.9	0.26	32.9	10.4	571.8	30.5	0.61
55	144.50	5.57	0.469	10.36	486	56.7	121.1	0.24	31.4	9.9	567.3	29.8	
63	179.30	5.60	0.480	10.78	490	58.3	128.1	0.23	33.6	10.8	571.8	30.6	
82	221.00	6.42	0.501	10.65	491	58.6	135.1	0.26	35.6	10.2	571.5	30.8	0.62
92		6.58	0.485	10.46	489	58.6	136.0	0.22	36.7	10.3	575.9	30.8	0.60
107	324.00	7.99	0.516	10.98	490	58.9	142.8	0.35	37.6	10.1	573.1	30.9	0.66
122	290.30	7.58	0.523	10.85	492	59.5	147.9	0.24	38.7	10.1	561.7	30.6	0.62
127	268.50	7.52	0.509	10.70	488	58.2	149.3	0.23	37.2	9.6	567.6	30.6	
134	277.90	8.03	0.531	10.88	491	59.3	151.1	0.23	40.2	9.9	573.3	31.2	0.65
142	293.00	8.33	0.532	10.99	489	59.1	153.7	0.23	41.0	9.9	572.3	30.8	0.64
153[a]	6.94	3.00	0.422	10.54	483	53.7	89.9	0.17	26.7	9.8	560.8	28.8	
162[a]	40.13	3.99	0.473	10.84	485	55.7	100.6	0.20	29.7	10.5	564.8	29.7	0.59

Note. Core location: 37°58.049′N; 26°5.489′W; gray areas indicate ash and tephra layers.
[a]Samples were contaminated with seawater.

(described above). According to the prior element concentration analyses (ICP-OES) individual sample amounts equivalent to ~1,500 ng Sr (usually in the range of tens to hundreds of µl pore water) were dried down in 2 ml of a 1 plus 2 mixture of 30% H_2O_2 (supra pure) and 8 N HNO_3 (double distilled from per analyses quality). The separation of Sr followed a highly selective one step ion exchange chromatography using SrSpec resin (Eichrom) at whole procedure blanks of max. 60 pg. Before loading 100 to 200 ng Sr mixed with $TaCl_5$ activator on Re single filaments for TIMS measurements the Sr eluate was dried down in the H_2O_2/HNO_3 mixture as described above. Repeated analyses of the standard NIST SRM 987 were used for performance monitoring and normalization of the measured $^{87}Sr/^{86}Sr$ ratios applying a standard value of 0.710248 and reaching a reproducibility of ±0.000010 (2 SD, $n = 10$) throughout the study. The latter level of precision is representative for the individual sample results (see uncertainties given in Table 2 and Table 4). Furthermore, the IAPSO seawater standard a $^{87}Sr/^{86}Sr$ ratio was determined on 0.709178 at ±0.000010 (2 SD, $n = 4$).

2.8. Ca Isotopes

Ca isotope measurements were performed on aliquots of the original pore water samples used for Sr isotope and element geochemistry ICP-OES analyses, with the same pretreatment as described for Sr purification. Calcium yields were >95% suggesting that Ca isotopes are not measurably fractionated by chemical purification (Morgan et al., 2011).

Prior to Ca isotope measurements samples were purified to remove matrix and interfering elements. We used a fully automated chromatographic purification system (prepFAST MC, ESI, Omaha, Nebraska, USA) following the method of Romaniello et al. (2015).

Calcium isotope measurements were performed on a MC-ICPMS (Thermo Scientific Neptune, Thermo Fisher Scientific, Bremen, Germany) at the mass spectrometer facilities of GEOMAR. The mass spectrometer was set up to measure m/z of 42, 43, 43.5, and 44 simultaneously. In order to suppress interfering Ca- and Ar-hydrides (e.g., $^{40}Ar^1H_2$ on ^{42}Ca) an APEX IR (ESI, Omaha, Nebraska, USA) sample introduction system was used. All measurements were performed in medium resolution (MR, m/Δm ~4,000) on the low mass side of the peaks (cf. Wieser et al., 2004).

Instrumental fractionation (mass bias) was corrected by applying the standard-sample-bracketing (SSB) approach. Interference correction for remaining sample Sr was done following the method of Morgan et al. (2011). Ca isotopes are given in the $\delta^{44/42}Ca$ notation, which represents the deviation of the sample

^{44}Ca/^{42}Ca from that of the international Ca standard NIST SRM 915a in per mil (‰). Long-term $\delta^{44/42}$Ca of the reference materials NIST SRM 915b (0.35 ± 0.11‰, 2 SD, $n = 13$), NIST SRM 1486 (-0.50 ± 0.05‰, 2 SD, $n = 131$) and IAPSO (0.89 ± 0.06‰, 2 SD, $n = 128$) agree well with the literature values. A procedural blank for the Ca isotope work was determined and found to contribute less than 1% of the processed Ca.

2.9. Mg Isotopes

Mg was separated from matrix elements by cation chromatography using DOWEX AG 50 W-X12 in polypropylene columns. Mg was eluted using HNO_3 (2 N). Splits (1 ml) before and after the Mg elution peak were screened for Mg as indicator for quantitative ion separation.

Mg isotope ratios were analyzed on a Neptune Plus MC-ICP-MS at Bundesanstalt für Materialforschung, Berlin. Samples and standards were introduced into a SIS spraychamber using a PFA microflow nebulizer with an uptake rate of 165 μl/min. Measurements were done in medium resolution mode using a normal sample cone and a X-skimmer cone. Procedural blanks are typically <7 ng Mg, of which <2 ng derived from the column procedure.

Measured Mg isotope ratios were normalized to the standard ERM-AE 144 (Vogl et al., 2016) to compensate for mass bias drift (i.e., SSB). Samples and standard were diluted in HNO_3 (0.32 M) to ≈ 0.75 μg/ml Mg, where matching was better than 12%. Isotope ratios are reported in the δ-notation, that is, as the deviation of a measured isotope intensity ratio (I) with the high mass isotopes $y = {}^{25}$Mg or $z = {}^{26}$Mg over the low mass-isotope ^{24}Mg of a sample (smp) from that of a standard (std):

$$\delta Mg^{y,z/24}_{std} = \frac{\left(\frac{I\left({}^{y,z}Mg\right)}{I\left({}^{24}Mg\right)}\right)_{smp} - \left(\frac{I\left({}^{y,z}Mg\right)}{I\left({}^{24}Mg\right)}\right)_{std}}{\left(\frac{I\left({}^{y,z}Mg\right)}{I\left({}^{24}Mg\right)}\right)_{std}} \tag{1}$$

δ values (abbreviated as δ^{25}Mg and δ^{26}Mg) were converted from the ERM-AE144 reference frame into the DSM3 reference frame using equation (Vogl & Pritzkow, 2010) for δ values obtained from the above equation in their basic form (no ‰, ppm, or else). When δ values in ‰ are to be used, they have to be divided by 1,000 before entering into the following equation.

$$\delta^{y,z/x}E(spl)_{std\ B} = \delta^{y,z/x}E(spl)_{std\ A} - \delta^{y,z/x}E(std\ B)_{std\ A} + \left(\delta^{y,z/x}E(spl)_{std\ A} \cdot \delta^{y,z/x}E(std\ B)_{std\ A}\right) \tag{2}$$

As quality control standards we have analyzed NASS-6 (North Atlantic Seawater, NRC Canada) and the reference material ERM-AE145. NASS-6 yields $\delta^{25}Mg_{DSM3} = -0.37 \pm 0.04$‰ and $\delta^{26}Mg_{DSM3} = -0.74 \pm 0.06$‰ (2 SD, $n = 4$), identical within 2 SD to the published values of NASS-5 by Wombacher et al. (2009) with $\delta^{25}Mg_{DSM3} = -0.43 \pm 0.07$‰ (2 SD, $n = 8$) and $\delta^{26}Mg_{DSM3} = -0.84 \pm 0.16$‰ (2 SD, $n = 4$). Our measurements of ERM-AE145 yield $\delta^{25}Mg_{DSM3} = -2.30 \pm 0.05$‰ and $\delta^{26}Mg_{DSM3} = -4.58 \pm 0.08$‰ (2 SD, $n = 3$), identical within 2 SD with published values in Vogl et al. (2016) with $\delta^{25}Mg_{DSM3} = -2.30$ ‰ and $\delta^{26}Mg_{DSM3} = -4.61$ ‰.

The uncertainty of δ-values for the entire dissolution, separation and measurement procedure is estimated to <0.1‰ (2 SD).

2.10. Head Space Gas Analyses

Headspace gas composition of 20-ml glass vials containing 3 cm^3 of sampled sediment and additional 6-ml NaCl-solution were prepared according to Sommer et al. (2009). The vials were stored upside down at room temperature until measurement by using gas chromatography at GEOMAR. One hundred microliters of headspace gas was injected into a Shimadzu gas chromatograph (GC-2014), equipped with flame ionization detector and thermal conductivity detector (carrier gas: He 5.0; HayeSepTM Q 80/100 column, column length: 2 m; column diameter: 1/8"). The detection limits for CH_4 and CO_2 were 0.1 ppmV and 100 ppmV, respectively. Precision was about 4 ‰ (2 SD).

Porewater concentrations of dissolved methane (mmol per liter porewater) were calculated by considering measured sediment porosity, molar volumes at laboratory pressure, and temperature. CO_2 values were used to determine pH values using the co2sys.xls program by Pelletier et al. (2005).

2.11. Endmember Calculations

Endmember (EM) calculations were performed for Mg, Ca, SO_4, and Sr, assuming binary mixing of seawater and the theoretical fluid EM. To calculate fluid EM we used element ratios versus elements for $^{87}Sr/^{86}Sr$ versus Sr, Mg/Sr versus Mg, Mg/Ca; Ca, and Mg/SO_4 versus SO_4. Seawater values were used as follows: $^{87}Sr/^{86}Sr = 0.709176$, $Sr = 90\ \mu M$, $SO_4 = 27.8\ mM$, $Ca = 10\ mM$, and $Mg = 53.2\ mM$. For the fluid EM, a fixed value is required, which is typically $Mg = 0$ for hydrothermal fluids. Since this is not possible in this case we approximate EM concentrations by using a fixed $^{87}Sr/^{86}Sr$ ratio (see details in section 4.6). For each element ratio versus element concentration we calculated a mixing line using the following equation (here shown for the example $^{87}Sr/^{86}Sr$ vs. Sr):

$$\frac{^{87}Sr}{^{86}Sr}_{mix} = \frac{f_b[Sr]_b \frac{^{87}Sr}{^{86}Sr}r_b + (1-f_b)[Sr]_a \frac{^{87}Sr}{^{86}Sr}r_a}{f_b[Sr]_b + (1-f_b)[Sr]_a} \tag{3}$$

A comprehensive list for all used element ratios with all data can be found in the supporting information.

2.12. Thermodynamic Model

The saturation state (SI) of caminite was calculated by comparing the ion activity product (IAP) of the solubility reaction to the corresponding thermodynamic equilibrium constant (K):

$$SI = \log\left(\frac{IAP}{K}\right). \tag{4}$$

The following stoichiometry was adopted for the dissolution reaction (Janecky & Seyfried, 1983):

$$MgSO_4\ 0.25Mg(OH)_2\ 0.2\ H_2O + 0.8\ H^+ \leftrightarrow 1.25\ Mg^{2+} + SO_4 + H_2O$$
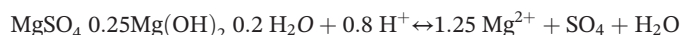
So that the equilibrium constant is defined as

$$K_{caminite} = \frac{a_{Mg}^{1.25} a_{SO_4}}{(10^{-pH})^{0.8}\ a_{H_2O}} \tag{5}$$

where a represents the species activitities.

To test the evolution of the saturation index over a broad temperature and pressure range, three different thermodynamic equilibrium constants (valid for a SO_4/Mg ratio of 0.625) were chosen from the work by Janecky and Seyfried (1983). In the lower temperature region $K_{caminite}$ equals 5.3 and is valid for 25 °C and 1 bar. For data points near 200 °C $K_{caminite}$ is assumed to be −1.98 and is valid for 200 °C and 500 bar and the SI for 300 °C uses the value −5.59 for the equilibrium constant and is valid for 300 °C and 500 bar.

Species activities were calculated based on the molal concentration (m) and the activitiy coefficient (γ):

$$a = \gamma\ m \tag{6}$$

The activity coefficients and the activity of water were computed based on the Pitzer model as described in and originally derived by Pitzer and Mayorga (1973). Interactions among the major sea ions were considered including Na, Mg, Ca, K, Cl, and SO_4 and their concentrations were set either to the bottom water values or the extrapolated endmember values. Respective Pitzer parameters were derived from internally consistent collections (Greenberg & Moller, 1989; Pabalan & Pitzer, 1987), which incorporate the effects of in pairing into their parameterization. It should be noted that the temperature range for the Pitzer data applied in the calculation of the species activities in most cases does not exceed 200 °C. Instead of extrapolating the
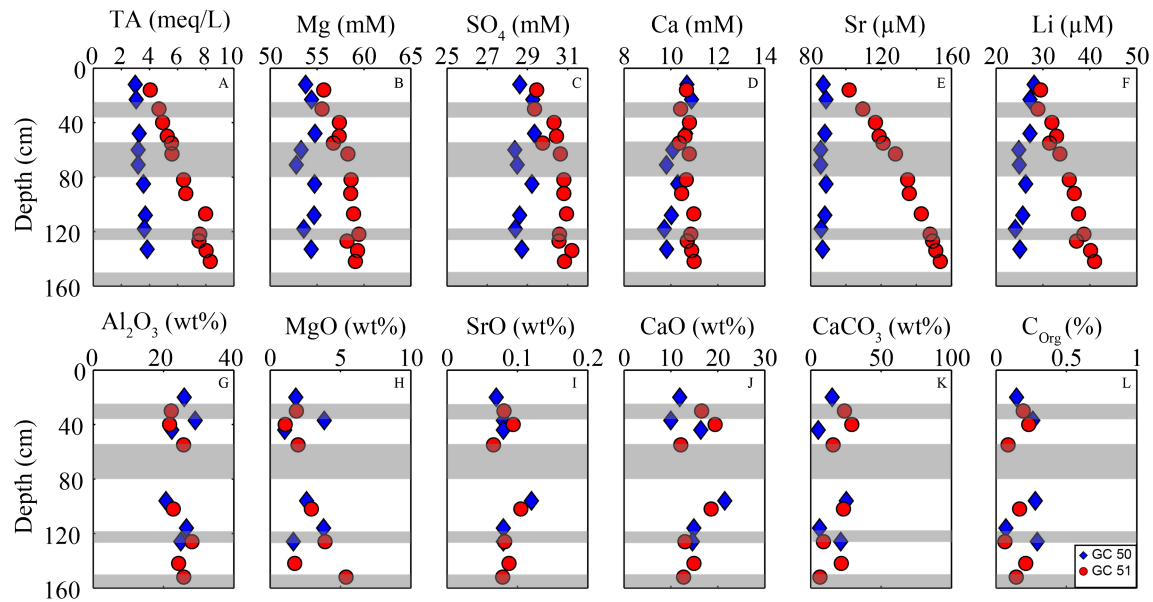
Figure 2. (a–f) Pore water profiles for Total Alkalinity, Mg, SO_4, Ca, Sr, and Li; (g–l) depth profiles for solids of Al_2O_3, MgO, SrO, CaO, $CaCO_3$, and C_{Org}; Gray area indicates ash layers based on GC51.

Pitzer parameters outside the stated temperature range, we use the parameterization of the upper temperature limit. For comparison, caminite SI is calculated for a range of pH values (7, 7.5, and 8). Also, while the equilibrium constants for elevated temperatures are valid only for 500 bar, we have also included the SI values that were calculated with activities for 1 bar to allow for a rough estimate of the pressure effect on the SI.

2.13. Transport Model

A simple 1-D transport model including diffusion and advection was applied using Mathematica 11.3 (Wolfram Research, 2018). The model was solved for the solute species Mg, Ca, TA, and SO_4. The general differential equation reads as follows:

$$\frac{\partial \phi \cdot C}{\partial t} = \frac{\partial \left(\phi \cdot D_s \cdot \frac{\partial C}{\partial x} \right)}{\partial x} - \frac{\partial (\phi \cdot v \cdot C)}{\partial x} \tag{7}$$

where t is the time (yr), x is the depth (cm), ϕ is the porosity (unitless), C is the concentration of solutes (mmol dm^{-3}), D_s is the diffusion coefficient in the sediments (cm^2 yr^{-1}) corrected for tortuosity after (Boudreau, 1997), and v is the fluid velocity (cm yr^{-1}). The model did not include any reactions. Initial porosity was set to 0.8, and porosity after compaction was set to 0.6 to fit the measured profile. Boundary conditions were defined for the sediment surface (0 cm) with ambient seawater concentrations (Mg = 54 mM, Ca = 10.2 mM, SO_4 = 28.7 mM, and TA = 2.7 meq/L), and for 300-cm depth (Mg = 63 mM, Ca = 11.5 mM, SO_4 = 33 mM, and TA = 11 meq/L; note that the lower boundary conditions are not equal to the calculated EM). The model was run into steady state. The upward flow velocity was determined by fitting the model to the measured pore water data.

2.14. Seismic Data

The reflection seismic data (Figure 1c) have been collected during RV *Meteor* expedition M79/2 (Hübscher, 2012). Four so-called GI-Guns created the seismic signal and a 144-channel, 600 m-long seismic streamer, with a channel spacing of 4.2 m, recorded the data. Processing included band-pass filtering, energy balancing, NMO-correction, stacking, time-migration, and fx-deconvolution. For an overview of the marine seismic method, see Hübscher and Gohl (2014).

Table 3
Isotope Results for $^{87}Sr/^{86}Sr$, $\delta^{34}S$, $\delta^{18}O_{SO4}$, $\delta^{26}Mg$, $\delta^{30}Si$, and $\delta^{44/42}Ca$ for GC50 and GC51

Depth (cm)	$^{87}Sr/^{86}Sr$	2 SD	n	$\delta^{34}S_{SO_4}$ [‰; V-CDT]	2 SD	n	$\delta^{18}O_{SO_4}$ [‰; V-SMOW]	2 SD	n	$\delta^{26/24}Mg$ [‰; DSM3]	2 SD	n	$\delta^{30}Si$ [‰; NBS28]	2 SD	n	$\delta^{44/42}Ca$ [‰; SRM915A]	2 SD	n
GC50																		
23	0.709061	0.000007	3	—	—	—	—	—	—	−0.80	0.06	3	1.63	0.15	2	0.88	0.07	4
133	0.708817	0.000010	4	24.2	0.08	2	15.9	0.46	2	−0.75	0.04	3	1.41	0.23	2	0.86	0.08	4
GC51																		
16	—	—	—	21.9	0.10	2	11.0	0.82	2	—	—	—	1.6	0.22	3	—	—	—
50	0.708084	0.000013	4	23.0	0.02	2	14.0	0.97	2	−0.39	0.04	3	1.79	0.22	3	0.84	0.08	4
82	0.707752	0.000010	4	—	—	—	—	—	—	−0.30	0.06	3	1.46	0.18	3	0.81	0.05	4
134	—	—	—	24.7	0.05	2	17.5	0.80	2	—	—	—	—	—	—	—	—	—
142	0.707428	0.000008	3	—	—	—	—	—	—	−0.18	0.05	3	1.22	0.08	2	0.77	0.05	4

3. Results

3.1. Pore Fluid Composition and Isotope Data

Pore fluid depth profiles for TA, Mg, Ca, SO$_4$, Li, and Sr are shown in Figures 2a–2f, and data are provided in Tables 1 (GC50) and 2 (GC51). The reference core GC50 shows a slightly elevated TA with 3.84 meq/L at 133 cm below seafloor (bsf). Ca is slightly decreasing from 10.86 at 12 cm bsf to 9.72 mM at 118 cm bsf. Sr is depleted in with respect to ambient bottom water (91 µM), with a decrease to 86.73 µM at 133 cm bsf. Mg, SO$_4$, and Li do not show any deviations from seawater values. For GC51, TA increases downcore from seawater values of 2.35 meq/L to up to 8.33 meq/L at 142 cm bsf. Also Mg is increasing with depth to 59.46 mM at 122 cm bsf, and SO$_4$ increases from 27.8 to 31.21 mM at 134 cm bsf Ca remains almost constant over depth, with a slight increase up to 10.99 mM at 142 cm bsf with respect to seawater (10.2 mM). Sr in GC51 increases up to 150 µM at 142 cm bsf. In addition to that Li is also increasing to 40 µM in GC 51.

Isotope systematics of GC51 show a strong deviation from seawater for $^{87}Sr/^{86}Sr$ and $\delta^{26}Mg$ and only minor deviations for $\delta^{34}S$, $\delta^{44/42}Ca$, and $\delta^{30}Si$ (Figure 4 and Table 3). $^{87}Sr/^{86}Sr$ shows a decreasing trend from 0.7091 (present-day seawater) to 0.7074 at 142 cm bsf. $\delta^{26}Mg_{GC51}$ values of the sampled fluids show an increase in $\delta^{26}Mg$ from −0.81‰ (seawater) to −0.18‰ at 142 cm bsf. $\delta^{34}S_{GC51}$ increases with depth from 21.9‰ at 16 cm bsf to 24.7‰ at 134 cm bsf. $\delta^{44/42}Ca_{GC51}$ does decrease slightly from 0.84‰ at 50 cm bsf to 0.77‰ at 142 cm bsf. $\delta^{30}Si_{GC51}$ does on the other side show no deviation from seawater values with depth. In contrast to GC 51 all isotopic ratios measured for GC50 do not show any or only minor ($^{87}Sr/^{86}Sr$ and $\delta^{34}S$) deviations from present day seawater values (Figure 4 and Table 3).

3.2. Solid Phase

The sediments largely consist of nannofossil-rich mud to mud-rich nannofossil ooze with variable admixture of fresh volcanic, siliciclastic, and biogenic material. A detailed description of sediments and components can be found in the supporting information. Organic input to sediments is low resulting in an average amount <0.3% of C$_{Org}$. CaCO$_3$ proportion of the sediments is in average ~20%. The main composition of the sediments is rather constant over depth and does not show pronounced differences between the two coring locations (Figures 2g–2l). The Chemical Index of Alteration (CIA; Nesbitt & Young, 1982) is used as a measure to determine the degree of weathering of the sediments. The CIA is calculated as follows: $CIA = Al_2O_3/(Al_2O_3 + CaO^* + Na_2O + K_2O) \times 100$. CaO* is the Ca bound to silicates and is determined by subtracting Ca bound to carbonates (CaCO$_3$ = 8.33 * TIC) from total Ca. The average CIA for both cores is between 40% and 60% (details can be found in the supporting information data).

3.3. Head Space Gas

Head space gas analyses for CH$_4$ and CO$_2$ did not show any variations with depth (see supporting information for data). CH$_4$ values stay at background values. The highest methane concentration was observed in GC50 at 166 cm bsf with 0.739 µM. In addition to that, also fCO$_2$ values remain at background values with slightly elevated values for GC51. fCO2 values go up to 5,599 ppm in GC51. The calculated pH values from fCO$_2$ and TA concentrations are for both cores about 7.5.

4. Discussion

In the following, we will present a comprehensive analysis of potential processes that might explain the unusual geochemical pore fluid signature of GC51 with anomalously high TA, Mg, and SO$_4$ concentrations.

4.1. Near-Surface Diagenetic Processes

Pore water profiles of enriched species display a slight exponential curvature within the uppermost ~50 cm (Figure 2). Generally, such type of profiles can either be the result of continuous reactive processes or be caused by fluid advection. Reactions typically include organic matter

degradation, secondary redox reactions, weathering/alteration of rocks, and mineral dissolution reactions. Our data suggest that the reactive influence in the shallow sediments is only minor: The TR in the Central North Atlantic Ocean receives only minor input of organic matter reflected by very low concentrations of TOC (<0.3 wt.%). Moreover, the increase in TA that results from organic matter degradation should also have been observed in GC50 where the increase is almost negligible. The increase in TA could also be explained by the anaerobic oxidation of methane (AOM) coupled to sulfate reduction. This would require a deep methane source, but neither indications for sulfate reduction (SO_4 concentrations are elevated in GC51) nor methane enrichment were detected in GC51. We assume that some of the elevated TA in GC51 comes from minor organic matter degradation, but additional processes have to be considered. Weathering/alteration of rocks or mineral dissolution processes could on first sight explain the curvature in the increasing profiles in GC51. Weathering of the volcaniclastic sediments can have an effect on the fluid composition, as minerals like Mg-smectite and zeolites can be formed or elements can be released due to volcanic glass dissolution (Schacht et al., 2008). However, visual analyses of the surface sediments by smear slides did not reveal indications for altered volcanic compounds or any secondary Mg or SO_4 bearing minerals (e.g., being indicative for hydrothermal alteration). Furthermore, the sediments of the reference core GC50 are identical in composition and depth of stratigraphic layers compared to GC51 (Figures 2g–2l). Intense weathering and formation of secondary minerals typically results in the loss of alkaline and alkaline earth metals, which is reflected in high values (>75%) of the CIA. CIA values for both cores do not show any evidence for pronounced alteration processes and no depth-related trends.

4.2. Indications for Upward Fluid Flow

The lack of evidence for alteration processes in the near-surface sediments suggests that the geochemical composition of the fluid is not the result of in situ processes but instead seems to be derived from deeper sources. The application of a simple numerical fluid transport model was carried out to test if the shape of the profiles (Figures 2a–2f) can be explained by an advective flux component. We tested two model scenarios (i) only diffusion and (ii) advection and diffusion (Figure 3). Indeed, a reasonably good fit to the data could be obtained with a fluid velocity of 0.5 cm yr^{-1}, emphasizing the need to include the advection process in the profile interpretation. With shallow diagenetic processes being only of minor importance, the hypothesis that fluids are derived from a deeper source is supported.

4.3. Hydrothermal Signature

With respect to the location close to an active spreading center and recent magmatic activity in the area, we suspect that the observed pore water anomalies are related to hydrothermal activity. Many processes in hydrothermal systems do affect Mg and SO_4 concentrations of fluids. Below, we analyze potential processes that might cause such anomalies and discuss their likeliness.

4.3.1. SO_2-Enriched Volatiles

Hydrothermal fluids enriched in Mg and SO_4 have been reported from other regions, for example, the DESMOS caldera (Gamo et al., 1997; Seewald et al., 2015). In these cases, the excess SO_4 concentrations were explained by the discharge of SO_2-enriched magmatic volatiles and their subsequent disproportionation to SO_4. Such highly acidic fluids can leach Mg-rich silicate minerals from the host rock, resulting in increased Mg concentrations (Gamo et al., 1997). Sulfur of magmatic origin can be distinguished from seawater sulfur and other sources by its $\delta^{34}S$ signature. Fluids sampled at the DESMOS caldera show much lower values compared to seawater and, hence, are typical for a mantle sulfur source ($\delta^{34}S_{Mantle} < 5‰$; Seewald et al., 2015). In contrast, $\delta^{34}S_{GC51}$ values increase slightly and stay at levels above seawater (Figure 4a). A mantle origin of SO_4 via disproportionation from SO_2 we can rule out.

4.3.2. Anhydrite Dissolution

One of the most abundant minerals formed in hydrothermal systems is anhydrite. Hydrothermal anhydrite formation is a major sink for SO_4, resulting in the removal of SO_4 from fluids (Alt, 1995). The mineral phase forms at temperatures above 150 °C but is generally not present in old, altered oceanic crust as it dissolves at lower temperatures (Alt, 1995). Dissolution of anhydrite could therefore be a source for SO_4 to the pore fluids (Gieskes et al., 2002). $\delta^{34}S$ values of anhydrite are typically around or slightly above seawater (Alt, 1995), matching our observations in the fluids (Figure 4a). In contrast, Ca concentrations are not significantly elevated in GC51, albeit the fact that anhydrite dissolution releases equal amounts of Ca and SO_4 to the pore fluids. Moreover, an extensive dissolution of anhydrite should result in much stronger deviations of the
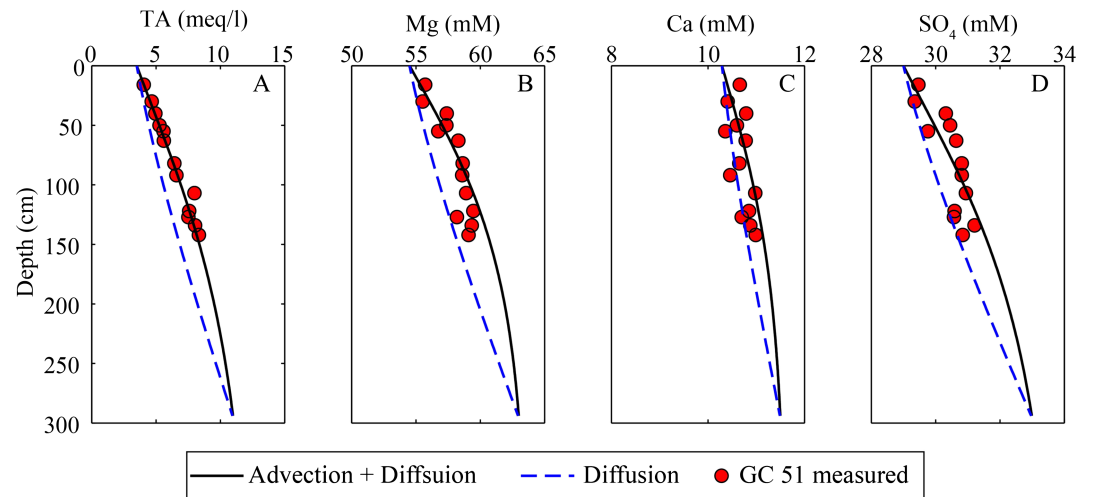
Figure 3. Transport model results for both scenarios: (i) diffusion (dashed line) and (ii) diffusion and advection (solid line) for (a) TA; (b) Mg; (c) Ca, and (d) SO₄.

$\delta^{44/42}Ca_{GC51} = 0.77‰$ from $\delta^{44/42}Ca_{Seawater} = 0.89‰$ (Figure 4b). Anhydrite has a shift of 0.5‰ from seawater to lower values (Amini et al., 2008). Thus, an additional sink for Ca, for example, calcium carbonate formation or ion exchange with clay minerals would be required or only a minor dissolution of anhydrite seems plausible here. Additionally, dissolution of anhydrite could explain the elevated Sr concentrations. Sr is an abundant trace element in hydrothermally formed anhydrite (Teagle et al., 1998). However, anhydrite dissolution cannot explain the increased TA or Mg concentration.

4.3.3. Mg-Rich Smectite

Mg-rich smectite, such as saponite, is the major sink for Mg in hydrothermal systems (Alt et al., 1986). In contrast to anhydrite, saponite is present in aged oceanic crust and is not dissolving during cooling of hydrothermal systems (Alt & Honnorez, 1984). Mg Smectite dissolution can be excluded as potential source for the Mg excess relative to seawater. Clay minerals do have a significant ion exchange capacity due to their large surface area. The main cations being exchanged are Mg, Ca, H, and Na (Wimpenny et al., 2014). Accordingly, smectite could be a potential sink for Ca and source for Mg. The overall $\delta^{26}Mg$ of Mg-smectites is above 0‰ (Figure 4c, Teng, 2017). Most of Mg is bound to the clay mineral lattice and only absorbed Mg in the interlayers can be exchanged. The exchangeable Mg of smectite is typically around −1.5‰ $\delta^{26}Mg$ (Wimpenny et al., 2014) and therefore lower than seawater values. Consequently, ion exchange should result in a decrease of the $\delta^{26}Mg$ value in the fluid relative to the $\delta^{26}Mg$ in seawater, which is opposite to the $\delta^{26}Mg$ values in GC51. In contrast, the dissolution of Mg-rich silicates by acidic fluids yields $\delta^{26}Mg$ values between −0.15‰ and −0.25‰ (Teng, 2017), identical with the pore fluid $\delta^{26}Mg$.in GC51.

Silicon isotopes ($\delta^{30}Si$) can be used as an additional fluid tracer, as different reservoirs are characterized by distinct $\delta^{30}Si$ values. Mantle fluids have an average $\delta^{30}Si$ value of −0.3‰ (De La Rocha et al., 2000). Also secondary clay mineral dissolution would enrich the fluid phase in light ^{28}Si, as clays show on average low $\delta^{30}Si$ values of −2.1‰ (De La Rocha et al., 2000; Ziegler et al., 2005; Opfergelt et al., 2010). The $\delta^{30}Si$values in GC51 range between +1.2‰ and +1.8‰ (Figure 4d) and thus overlap within error of the Si isotope value of the deep Atlantic water at 2,800 m water depth (average $\delta^{30}Si_{Atlantic} = +1.6‰$ (Brzezinski & Jones, 2015; De Souza et al., 2012), and the reference core GC50, which has an average $\delta^{30}Si$ value of +1.5‰ (see Table 3). Consequently, dissolution of secondary Si-rich minerals or mixing with mantle fluids can be excluded as well.

4.3.4. Low-Temperature Weathering of Peridotite

Snow and Dick (1996) proposed that the weathering of peridotite at temperatures below 150 °C results in the pervasive loss of Mg of the basement. Slow-spreading ridges are the typical environments were peridotites get exposed to the seafloor surface. Ligi et al. (2013) proposed that the increase in number of slow-spreading ridges in the past 80 Ma have contributed to a shift in the global Mg cycle as enhanced weathering of peridotites could have occurred. However, up to date no Mg-rich fluids have been found in slow-
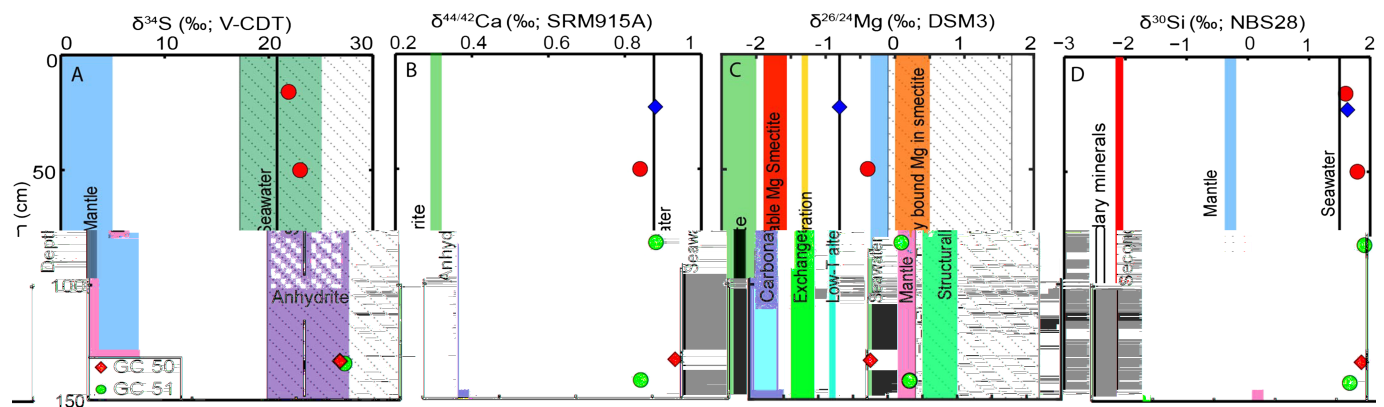
Figure 4. Depth profiles for isotopes and potential sources; the shaded area in (a) and (b) represents the estimated range of $\delta^{26}Mg$ and $\delta^{34}S$-values of caminite. (a) $\delta^{34}S_{Seawater} = 21‰$; $\delta^{34}S_{Evaporites} = 19–25‰$; $\delta^{34}S_{Mantle} = 0–5‰$ (Alt, 1995); (b) $\delta^{26}Mg_{Seawater} = 0.81‰$, $\delta^{26}Mg_{Carbonate} < −2‰$, mantle = −0.4 to −0.2‰ (Teng, 2017); $\delta^{26}Mg_{exchangeable\ of\ smectite} = −1,5‰$; $\delta^{26}Mg_{structurally\ bound\ in\ smectite} = 0–0.5‰$ (Wimpenny et al., 2014); $\delta^{26}Mg_{Low-T\ alteration\ fluids} = −1.31‰$ (Liu et al., 2017); (c) $\delta^{30}Si_{Seawater} = +1.6‰$, $\delta^{30}Si_{Mantle} = −0.3‰$, $\delta^{30}Si_{Secondary\ Mineral} = −2.1‰$; (d) $\delta^{44/42}Ca_{Seawater} = 0.9‰$, $\delta^{44/42}Ca_{Anhydrite} = 0.3‰$, the shaded area in (a) and (c) indicates the presumed isotopic composition for caminite.

spreading environments. The hyperslow spreading TR could be suitable for the conditions defined for high Mg vents by Ligi et al. (2013). The crustal thickness of the basaltic Azores Plateau is about 14 km (Escartín et al., 2001), and exposure of mantle peridotite is unlikely here. In addition to that, no description of exposed peridotites is available for the TR. Nevertheless, if a deep fluid circulation could reach peridotites, low temperature weathering of peridotites results in the formation of Mg-smectite, accompanied with a fractionation of Mg isotopes (Liu et al., 2017). According to the authors fluids enriched in Mg affected by low-temperature weathering result in $\delta^{26}Mg$ values lower than seawater by −1.31‰, while $\delta^{26}Mg$ values in core GC51 are enriched with respect to seawater. Hence, we conclude that this process is not or at least not significantly affecting the fluid composition at GC51.

4.4. Dissolution of Caminite

None of the processes described above can satisfactorily explain the geochemical pore fluid anomalies of high Mg, SO_4, and TA concentrations observed in GC51. All of the above discussed processes only impact one of the three enriched species. A complex succession of these processes can also not satisfactorily explain the fluid geochemistry at GC51. We suggest therefore that we see here as of yet underestimated case where the dissolution of the hydrothermally formed mineral caminite may offer an explanation for the observed pore fluid deviations. Caminite is a magnesium-sulfate-hydroxide-hydrate ($MgSO_4$ 0.25 Mg $(OH)_2$ $0.2H_2O$), which to date has been only found once in a natural environment. Haymon and Kastner (1986) reported caminite from a black smoker site on the East Pacific Rise 21°N, precipitating directly from heated seawater. Furthermore, this mineral has been synthesized under laboratory conditions (Janecky & Seyfried, 1983). Both studies indicate that high fluid temperatures of >240 °C are needed to form caminite. Although caminite can be regarded as a rare mineral, Haymon and Kastner (1986) proposed that it could be an abundant mineral in hydrothermal recharge zones where high temperatures are present in the system while Mg-smectite formation is largely inhibited. The authors assumed that such a scenario is possible in hydrothermal systems with little fresh basaltic glass present in the recharge zone. This implies that during a former hydrothermal alteration Mg-smectite already formed and the reactivity of the basement is lower compared to young oceanic basement. The basement of the Azores Plateau has undergone intensive alteration (Beier et al., 2019); hence, there is the possibility that smectite formation has occurred before and no fresh basaltic glass is present at this location in the basement. Moreover, an enrichment of Li in fluids is indicative for elevated fluid temperatures in the subsurface (e.g., Scholz et al., 2010). The Li concentrations in GC51 are slightly elevated compared to the reference core; we can therefore assume that high fluid temperatures are present in the subsurface in the TR.

Thus, the general conditions for the formation of caminite (as defined by Haymon & Kastner, 1986) are likely to be met in the TR. It has also been shown that caminite dissolves rapidly at temperatures <240 °C

(Haymon & Kastner, 1986). Decreasing temperatures after hydrothermal activity could result in the dissolution of previously formed caminite increasing the Mg and SO_4 concentrations in the ambient fluids. This is also in line with the additional increased TA in GC51 compared to GC50 due to the release of $(OH)^-$ through the dissolution of caminite.

According to Janecky and Seyfried (1983), caminite is present in two modifications with different SO_4/Mg ratios. The authors describe one modification with $SO_4/Mg = 0.625$, which is the more stable phase at temperatures above 300 °C and pressures below 500 bars, and caminite with $SO_4/Mg = 0.7$, which is more stable at temperatures below 300 °C and 500 bars. In addition the $SO_4/(OH)^-$ ratio can vary between 1.25 and 2. Maximum concentrations of Mg and SO_4 in GC51 are above seawater levels by are 5.89 and 3.41 mM, respectively. To determine the excess TA at GC51, the maximum TA at GC50 was subtracted from the value at GC51, resulting in an excess concentration of 4.24. The resulting ratios for SO_4/Mg and $SO_4/(OH)^-$ are 0.58 and 0.8, respectively. These ratios are very similar to the published ratios despite the fact that minor modification of fluids in the remaining sedimentary column (e.g., through microbial activity) are possible.

Unfortunately, all isotope systems discussed in the preceding sections cannot be used to further constrain the process of caminite dissolution, which is simply due to the fact that no isotopic analyses for caminite have been reported so far. Hence, the measured isotopic compositions of $\delta^{26}Mg$ and $\delta^{34}S$ in GC51 provide a first idea of how these isotope systems are affected during formation of caminite. Based on our findings, we expect a shift toward positive $\delta^{34}S$ values, similar to anhydrite (Figure 4a), and a fractionation toward positive ^{26}Mg values (Figure 4c).

Caminite redissolution can explain the increase of Mg, SO_4, and TA in pore water of GC51, but elevated Sr concentrations remain a puzzling observation. In laboratory experiments caminite did not incorporate Sr into the mineral structure (Janecky & Seyfried, 1983). The absence of Sr in caminite thus indicates that the enrichment of Sr in pore fluids cannot be explained by caminite dissolution. Notably though, caminite is typically associated with anhydrite (Haymon & Kastner, 1986), which incorporates Sr and other divalent ions (Teagle et al., 1998). As discussed before, an accompanied minor dissolution of anhydrite could explain the Sr increase. Also, a small increase in Sr from anhydrite dissolution would have a minor affect SO_4 and Ca concentrations, as they have different concertation levels in the pore fluid. Thus, the suggested fluid mixture is generated by different sources but in the same depth and transported to the seafloor. Concentrations of Sr, Mg, Ca, and SO_4 are coherent and Sr can therefore be used as a tracer for EM calculation.

4.5. Endmember Calculation

The fluids sampled in GC51 are a mixture of ambient pore water (seawater) and the deep fluid. EM calculations are used to determine maximum concentrations of the fluid source. For hydrothermal fluids this is in general performed using a 0-mM EM for Mg and calculate respective element enrichments or depletions accordingly (e.g., Douville et al., 2002). However, the high Mg concentrations complicate the problem, and a workaround had to be found to constrain the unknown fluid endmember at depth. The concentrations of Sr, Mg, Ca, and SO_4 are coherent as the fluid mixture (from caminite and to a lower extent anhydrite dissolution) is generated in the same region and transported to the seafloor. We chose to base our estimates on $^{87}Sr/^{86}Sr$ ratios. Sr isotopes and concentration (1/Sr) plot on a linear regression line. The minimum isotope ratio can be approached for 1/Sr approaching toward 0, resulting in an $^{87}Sr/^{86}Sr$ of 0.7049 for GC51 (Figure 5c). Interestingly, this value is in agreement with ratios of the oceanic basement in the TR (0.7035 to 0.7060; Beier et al., 2008; White et al., 1976). Sr isotope ratios in the west are lower and shifting to higher ratios to the east. The sample location of GC51 is located in the part of the TR where values for $^{87}Sr/^{86}Sr$ are around 0.705. Moreover, the proposed EM value represents also Sr isotope ratios of hydrothermally formed anhydrite (Teagle et al., 1998). Assuming Sr release is caused by minor anhydrite dissolution as discussed before, this Sr release can also cause the Sr isotope deviation. Therefore, we take $^{87}Sr/^{86}Sr = 0.7049$ as a fixed EM for the following EM calculation of the other elements. The EM calculation was then performed as described in section 2.11 assuming a binary mixing of seawater and the EM. The best fit for $^{87}Sr/^{86}Sr$ versus Sr could be obtained with a Sr concentration of 650 μM. On a mixing line between seawater ($^{87}Sr/^{86}Sr = 0.709176$; Sr = 91 μM) and fluid EM ($^{87}Sr/^{86}Sr = 0.7049$; Sr = 650 μM) the measured sample lies at 10% EM fluid (Figure 5c). Accordingly, we used in a next step the Sr concertation as a fixed value and deduced the Mg concentration using the Sr/Mg ratio. The same approach was used to deduce EM Ca and SO_4
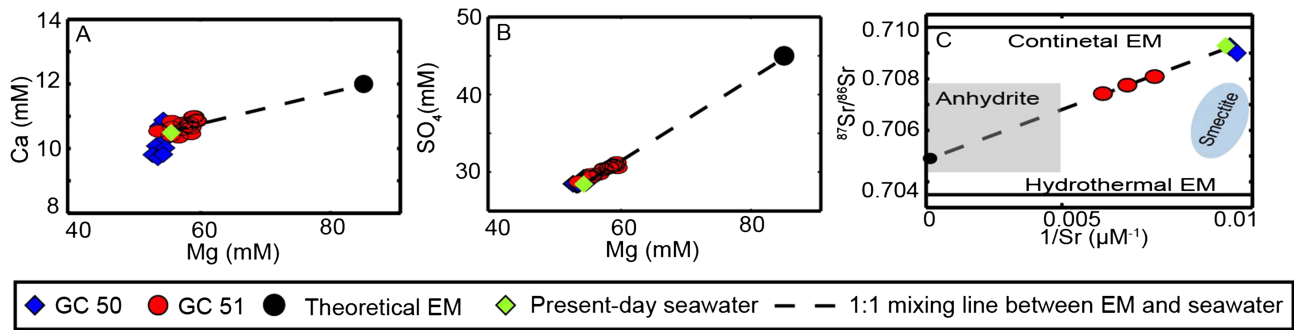
Figure 5. Binary mixing between present-day seawater (green diamond) and theoretical EM (black dots); dashed line: mixing line between seawater and EM; (a) Ca versus Mg; (b) SO_4 versus Mg; (c) $^{87}Sr/^{86}Sr$ versus 1/Sr, Anhydrite $^{87}Sr/^{86}Sr = 0.745–0.708$, 1/Sr < 0.005 (Teagle et al., 1998); Smectite $^{87}Sr/^{86}Sr = 0.705–0.707$, 1/Sr = 0.01–0.025 (Hart & Staudigel, 1980); Hydrothermal EM < 0.704 (Palmer & Edmond, 1989).

concentrations. The resulting EMs are as follows: Mg = 85 mM, SO_4 = 47 mM, Sr = 650 μM, Ca 12 = mM, and $^{87}Sr/^{86}Sr$ = 0.7049 (Figure 5). Nevertheless, this method is based on a number of assumptions (e.g., no modification of fluids in the sediment column), which cannot be further constrained, and hence, the EM calculation can only be regarded as a rough approximation.

Finally, we apply thermodynamic calculations to test the plausibility of the proposed scenario. The caminite saturation index—based on Pitzer-derived activities (Pitzer & Mayorga, 1973)—is calculated for seawater and the theoretical EM concentrations. The results in Figure 6 show that seawater and EM are strongly undersaturated in the low-temperature region and that both solutions are around the state of saturation at temperatures around 200°. Temperatures above 200 °C likely induce strong oversaturation. The similarity in SI values for seawater and EM stems from the fact that while SO_4 and Mg concentrations increase in EM solutions, their activity coefficient decreases compared to seawater. Variations in pH between 7 and 8 do not significantly influence the SI region for a given temperature and do not influence the overall interpretation. The good agreement between the calculated fluid EM and caminite solubility at elevated temperatures supports the theory that caminite controls the fluid composition at depth. Taking everything together, caminite dissolution offers the most plausible explanation for the seen fluid deviations in GC51.
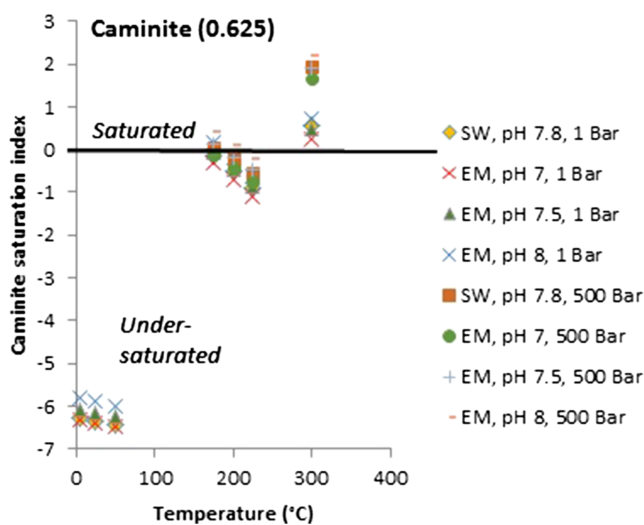

Figure 6. Saturation index for caminite (0.625; Janecky & Seyfried, 1983) at varying temperatures for seawater and fluid EM concentrations. For comparison, calculations are shown over a pH range of 7 to 8 and up to 500 bar, highlighting the importance of the temperature effect over the influence of pH and pressure.

4.6. Implications

The presence of caminite confirms the existence of a deep submarine hydrothermal system in the TR, which has not been reported yet in this region. Listric faults offer suitable fluid pathways, and advective fluxes, albeit low (0.5 cm/yr), imply an ongoing fluid circulation in the basement Dissolution of Caminite occurs when temperatures in hydrothermal systems drop below 240 °C. Our conclusion is that the system is currently in a waning state. Our conceptual model (Figure 7a) is based on the idea that a magma intrusion in the basement below the volcanic cone is currently cooling and the isotherms are retracting. Fluids circulating through the basement may dissolve caminite at temperatures <240 °C, but temperatures are still high enough to drive active fluid convection. Fluids affected by caminite dissolution are transported along the listric faults via diffusion and slow advection through the sediments to the surface (Figure 7b). The fact that caminite starts to dissolve rapidly when temperatures drop it might explain why it has been rarely reported to date. Our findings support the hypothesis by Haymon and Kastner (1986) that caminite can be abundant under specific conditions in hydrothermal recharge zones. To date, only for one further vent, at Brother lower cone (Kermadec arc, SW Pacific), caminite dissolution has been hypothesized to play a role in fluid generation (Kleint et al., 2019). Numerous
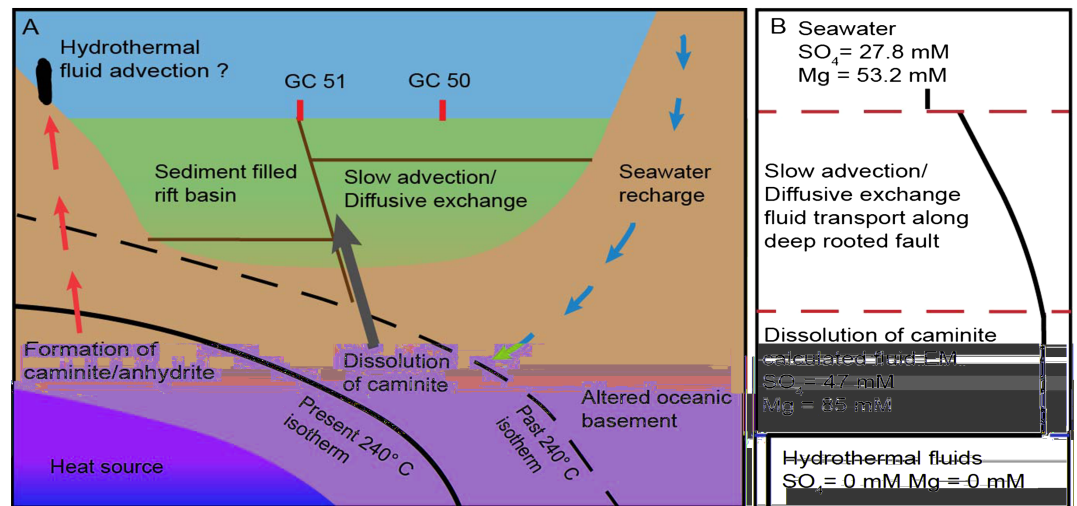
Figure 7. (a) Schematic model illustrating evolution of the hydrothermal system. The cooling heat source leads to a retraction of the 240 °C isotherm, forcing caminite out of the stability field. Ongoing recharge of seawater dissolves caminite and supports fluid flow along listric faults to the seafloor (b) Theoretical depth profile for dissolved SO_4 and Mg concentrations in the subsurface.

hydrothermal vents exist in slow-spreading settings, for example, Southwest Indian Ridge (German et al., 1998), but for none of them high Mg/SO_4 fluids have been reported. However, crustal age and geological setting would be favorable to host this type of vents. For the TR, 251 magmatic intrusions and submarine volcanoes in aged oceanic crust have been reported (Weiß et al., 2015), providing potentially suitable conditions for a widespread formation and dissolution of caminite.

5. Summary and Conclusions

We present pore fluid data from a gravity core taken at the rim of a submarine lava flow in the TR, which are characterized by high Mg, SO_4, and total alkalinity concentrations. By applying comprehensive isotope measurements and numerical modeling, we could exclude several known diagenetic and hydrothermal processes to cause the observed deviations. The most straightforward explanation for our findings is the dissolution of hydrothermally formed caminite. The literature offers little information on caminite, but it has been proposed that it can precipitate under specific conditions in hydrothermal recharge zones, which are generally met in the TR. Thus, our findings support the hypothesis by Haymon and Kastner (1986) suggesting that caminite occurrence could be more common than previously thought, especially in active hydrothermal systems before subsiding temperatures induce rapid caminite dissolution. This hydrothermal signal is the first indication of a deep submarine hydrothermal system in the TR. Hydrothermal systems are important sinks for Mg in the global budget (Mottl & Wheat, 1994). A widespread dissolution of caminite in cooling hydrothermal systems might cause a nonnegligible reflux of Mg to the ocean. The additional strong fractionation measured for $\delta^{26}Mg$ isotopes implies neglected effects on the oceanic Mg budget and seawater $\delta^{26}Mg$.

References

Albarède, F., & Beard, B. (2004). Analytical methods for non-traditional isotopes. *Reviews in mineralogy and geochemistry*, 55(1), 113–152.
Alt, J. C. (1995). Sulfur isotopic profile through the oceanic crust: Sulfur mobility and seawater-crustal sulfur exchange during hydrothermal alteration. *Geology*, 23, 585–588.
Alt, J. C., & Honnorez, J. (1984). Alteration of the upper oceanic crust, DSDP site 417: mineralogy and chemistry. *Contributions to Mineralogy and Petrology*, 87, 149–169.
Alt, J. C., Honnorez, J., Laverne, C., & Emmermann, R. (1986). Hydrothermal alteration of a 1 km section through the upper oceanic crust, Deep Sea Drilling Project Hole 504B: Mineralogy, chemistry and evolution of seawater-basalt interactions. *Journal of Geophysical Research*, 91, 10,309–10,335.
Amini, M., Eisenhauer, A., Böhm, F., Fietzke, J., Bach, W., Garbe-Schönberg, D., et al. (2008). Calcium isotope (δ44/40Ca) fractionation along hydrothermal pathways, Logatchev field (Mid-Atlantic Ridge, 14°45′N). *Geochimica et Cosmochimica Acta*, 72, 4107–4122.

Beaulieu, S. E., Baker, E. T., German, C. R., & Maffei, A. (2013). An authoritative global database for active submarine hydrothermal vent fields. *Geochemistry, Geophysics, Geosystems*, *14*, 4892–4905.

Beier, C. (2016). Azores Plateau—Cruise No. M128—July 2–July 27, 2016—Ponta Delgada (Azores, Portugal)—Ponta Delgada (Azores, Portugal), METEOR Berichte, p. 42.

Beier, C., Bach, W., Busch, A. V., Genske, F. S., Hübscher, C., & Krumm, S. H. (2019). Extreme intensity of fluid-rock interaction during extensive intraplate volcanism. *Geochimica et Cosmochimica Acta*, *257*, 26–48.

Beier, C., Haase, K. M., Abouchami, W., Krienitz, M. S., & Hauff, F. (2008). Magma genesis by rifting of oceanic lithosphere above anomalous mantle: Terceira Rift, Azores. *Geochemistry, Geophysics, Geosystems*, *9*, Q12013. https://doi.org/10.1029/2008GC002112

Boudreau, B. P. (1997). *Diagenetic models and their implementation: Modelling transport and reactions in aquatic sediments*. Berlin, Heidelberg, Berlin, Heidelberg, New York: Springer.

Butterfield, D. A., McDuff, R. E., Franklin, J., & Wheat, C. G. (1994). Geochemistry of hydrothermal vent fluids from Middle Valley, Juan de Fuca Ridge. Proceedings of the Ocean Drilling Program, Scientific Results Vol. 139.

Cardigos, F., Colaço, A., Dando, P. R., Ávila, S. P., Sarradin, P. M., Tempera, F., et al. (2005). Shallow water hydrothermal vent field fluids and communities of the D. João de Castro Seamount (Azores). *Chemical Geology*, *224*, 153–168.

Couto, R.P., Rodriguesa, A.S. and Neto, A.I. (2015) Shallow-water hydrothermal vents in the Azores (Portugal). Revista de Gestão Costeira Integrada-Journal of Integrated Coastal Zone Management 15.

Decker, J., & Helmold, K. P. (1985). The effect of grain size on detrital modes: A test of the Gazzi-Dickinson point-counting method: Discussion. *Journal of Sedimentary Research*, *55*.

Douville, E., Charlou, J., Oelkers, E., Bienvenu, P., Colon, C. J., Donval, J., et al. (2002). The rainbow vent fluids (36 14′ N, MAR): The influence of ultramafic rocks and phase separation on trace metal content in Mid-Atlantic Ridge hydrothermal fluids. *Chemical Geology*, *184*, 37–48.

Elderfield, H., & Schultz, A. (1996). Mid-Ocean Ridge hydrothermal fluxes and the chemical composition of the ocean. *Annual Review of Earth and Planetary Sciences*, *24*, 191–224.

Escartin, J., Cannat, M., Pouliquen, G., Rabain, A., & Lin, J. (2001). Crustal thickness of V-shaped ridges south of the Azores: Interaction of the Mid-Atlantic Ridge (36–39 N) and the Azores hot spot. *Journal of Geophysical Research*, *106*, 21,719–21,735.

Gamo, T., Okamura, K., Charlou, J.-L., Urabe, T., Auzende, J.-M., Ishibashi, J., et al. (1997). Acidic and sulfate-rich hydrothermal fluids from the Manus back-arc basin, Papua New Guinea. *Geology*, *25*, 139–142.

Georg, R., Reynolds, B. C., Frank, M., & Halliday, A. N. (2006). New sample preparation techniques for the determination of Si isotopic compositions using MC-ICPMS. *Chemical Geology*, *235*, 95–104.

German, C., Baker, E., Mevel, C., & Tamaki, K. (1998). Hydrothermal activity along the southwest Indian ridge. *Nature*, *395*, 490.

Gieskes, J.M., Gamo, T. and Brumsack, H. (1991) Chemical methods for interstitial water analysis aboard JOIDES resolution.

Gieskes, J. M., Simoneit, B. R. T., Shanks, W. C. III, Goodfellow, W. D., James, R. H., Baker, P. A., & Ishibashi, J.-i. (2002). Geochemistry of fluid phases and sediments: Relevance to hydrothermal circulation in Middle Valley, ODP Legs 139 and 169. *Applied Geochemistry*, *17*, 1381–1399.

Greenberg, J. P., & Moller, N. (1989). The prediction of mineral solubilities in natural waters: A chemical equilibrium model for the Na-K-Ca-Cl-SO$_4$-H$_2$O system to high concentration from 0-250 °C. *Geochimica et Cosmochimica Acta*, *53*, 2503–2518.

Gruen, G., Weis, P., Driesner, T., Heinrich, C. A., & de Ronde, C. E. (2014). Hydrodynamic modeling of magmatic–hydrothermal activity at submarine arc volcanoes, with implications for ore formation. *Earth Planet. Sci. Lett.*, *404*, 307–318.

Hart, S. and Staudigel, H. (1980) 43. Ocean crust-sea water interaction: Sites 417 and 418, Proceedings of the Ocean Drilling Program: Initial report. National Science Foundation, p. 1169.

Haymon, R. M., & Kastner, M. (1986). Caminite; a new magnesium-hydroxide-sulfate-hydrate mineral found in a submarine hydrothermal deposit, East Pacific Rise, 21 degrees N. *American Mineralogist*, *71*, 819–825.

Hensen, C., Nuzzo, M., Hornibrook, E., Pinheiro, L. M., Bock, B., Magalhães, V. H., & Brückmann, W. (2007). Sources of mud volcano fluids in the Gulf of Cadiz—Indications for hydrothermal imprint. *Geochimica et Cosmochimica Acta*, *71*, 1232–1248.

Hübscher, C. (2012) RV METEOR, Cruise Report M79/L2. August 26–September 21, 2009, Ponta Delgada (Azores/Portugal)–Las Palmas (Canary Islands/Spain). Institut für Geophysik.

Hübscher, C., & Gohl, K. (2014). Reflection/refraction seismology. In J. Harff, M. Meschede,S. Petersen, & J. Thiede (Eds.), *Encyclopedia of Marine Geosciences*. Dordrecht: Springer.

Humphris, S. E., & Thompson, G. (1978). Hydrothermal alteration of oceanic basalts by seawater. *Geochimica et Cosmochimica Acta*, *42*, 107–125.

Janecky, D., & Seyfried, W. (1983). The solubility of magnesium-hydroxide sulfate-hydrate in seawater at elevated temperatures and pressures. *American Journal of Science*, *283*, 831–860.

Kleint, C., Bach, W., Diehl, A., Fröhberg, N., Garbe-Schönberg, D., Hartmann, J. F., et al. (2019). Geochemical characterization of highly diverse hydrothermal fluids from volcanic vent systems of the Kermadec intraoceanic arc. *Chemical Geology*, *528*, 119289.

Ligi, M., Bonatti, E., Cuffaro, M., & Brunelli, D. (2013). Post-Mesozoic rapid increase of seawater Mg/Ca due to enhanced mantle-seawater interaction. *Scientific reports*, *3*, 2752.

Liu, P.-P., Teng, F.-Z., Dick, H. J. B., Zhou, M.-F., & Chung, S.-L. (2017). Magnesium isotopic composition of the oceanic mantle and oceanic Mg cycling. *Geochimica et Cosmochimica Acta*, *206*, 151–165.

Morgan, J. L., Gordon, G. W., Arrua, R. C., Skulan, J. L., Anbar, A. D., & Bullen, T. D. (2011). High-precision measurement of variations in calcium isotope ratios in urine by multiple collector inductively coupled plasma mass spectrometry. *Analytical chemistry*, *83*(18), 6956–6962. https://doi.org/10.1021/ac200361t

Nesbitt, H. W., & Young, G. (1982). Early Proterozoic climates and plate motions inferred from major element chemistry of lutites. *Nature*, *299*, 715.

Pabalan, R. T., & Pitzer, K. S. (1987). Thermodynamics of concentrated electrolyte mixtures and the prediction of mineral solubilities to high temperatures for mixtures in the system Na-K-Mg-Cl-SO$_4$-OH-H$_2$O. *Geochimica et Cosmochimica Acta*, *51*, 2429–2443.

Palmer, M. R., & Edmond, J. M. (1989). The strontium isotope budget of the modern ocean. *Earth Planet. Sci. Lett.*, *92*, 11–26.

Pelletier, G., Lewis, E., & Wallace, D. (2005). *A calculator for the CO$_2$ system in seawater for Microsoft Excel/VBA. Washington State Department of Ecology*. WA, Brookhaven National Laboratory, Upton, NY: Olympia.

Pitzer, K. S., & Mayorga, G. (1973). Thermodynamics of electrolytes. II. Activity and osmotic coefficients for strong electrolytes with one or both ions univalent. *The Journal of Physical Chemistry*, *77*, 2300–2308.

Reynolds, B. C., Aggarwal, J., Andre, L., Baxter, D., Beucher, C., Brzezinski, M. A., et al. (2007). An inter-laboratory comparison of Si isotope reference materials. *Journal of Analytical Atomic Spectrometry*, *22*(5), 561–568.

Romaniello, S., Field, M., Smith, H., Gordon, G., Kim, M., & Anbar, A. (2015). Fully automated chromatographic purification of Sr and Ca for isotopic analysis. *Journal of Analytical Atomic Spectrometry*, *30*, 1906–1912.

Schacht, U., Wallmann, K., Kutterolf, S., & Schmidt, M. (2008). Volcanogenic sediment-seawater interactions and the geochemistry of pore waters. *Chemical Geology*, *249*, 321–338.

Scholz, F., Hensen, C., De Lange, G. J., Haeckel, M., Liebetrau, V., Meixner, A., et al. (2010). Lithium isotope geochemistry of marine pore waters—Insights from cold seep fluids. *Geochimica et Cosmochimica Acta*, *74*, 3459–3475.

Scholz, F., Hensen, C., Reitz, A., Romer, R. L., Liebetrau, V., Meixner, A., et al. (2009). Isotopic evidence (^{87}Sr/^{86}Sr, δ^7Li) for alteration of the oceanic crust at deep-rooted mud volcanoes in the Gulf of Cadiz, NE Atlantic Ocean. *Geochimica et Cosmochimica Acta*, *73*, 5444–5459.

Scholz, F., Löscher, C. R., Fiskal, A., Sommer, S., Hensen, C., Lomnitz, U., et al. (2016). Nitrate-dependent iron oxidation limits iron transport in anoxic ocean regions. *Earth Planet. Sci. Lett.*, *454*, 272–281.

Seewald, J. S., Reeves, E. P., Bach, W., Saccocia, P. J., Craddock, P. R., Shanks, W. C., et al. (2015). Submarine venting of magmatic volatiles in the Eastern Manus Basin, Papua New Guinea. *Geochimica et Cosmochimica Acta*, *163*, 178–199.

Sommer, S., Linke, P., Pfannkuche, O., Schleicher, T., Deimling, J. S. V., Reitz, A., et al. (2009). Seabed methane emissions and the habitat of frenulate tubeworms on the Captain Arutyunov mud volcano (Gulf of Cadiz). *Marine Ecology Progress Series*, *382*, 69–86.

Teagle, D. A. H., Alt, J. C., & Halliday, A. N. (1998). Tracing the chemical evolution of fluids during hydrothermal recharge: Constraints from anhydrite recovered in ODP Hole 504B. *Earth and Planetary Science Letters*, *155*, 167–182.

Teng, F.-Z. (2017). Magnesium isotope geochemistry. *Reviews in Mineralogy and Geochemistry*, *82*, 219–287.

Van der Plas, L., & Tobi, A. (1965). A chart for judging the reliability of point counting results. *American Journal of Science*, *263*, 87–90.

Vogl, J., Brandt, B., Noordmann, J., Rienitz, O., & Malinovskiy, D. (2016). Characterization of a series of absolute isotope reference materials for magnesium: Ab initio calibration of the mass spectrometers, and determination of isotopic compositions and relative atomic weights. *Journal of Analytical Atomic Spectrometry*, *31*, 1440–1458.

Vogl, J., & Pritzkow, W. (2010). Isotope reference materials for present and future isotope research. *Journal of Analytical Atomic Spectrometry*, *25*, 923–932.

Vogt, P. R., & Jung, W. Y. (2004). The Terceira Rift as hyper-slow, hotspot-dominated oblique spreading axis: A comparison with other slow-spreading plate boundaries. *Earth Planet. Sci. Lett.*, *218*, 77–90.

von Eynatten, H., & Gaupp, R. (1999). Provenance of Cretaceous synorogenic sandstones in the Eastern Alps: Constraints from framework petrography, heavy mineral analysis and mineral chemistry. *Sedimentary Geology*, *124*, 81–111.

Weiß, B. J., Hübscher, C., Wolf, D., & Lüdmann, T. (2015). Submarine explosive volcanism in the southeastern Terceira Rift/São Miguel region (Azores). *Journal of Volcanology and Geothermal Research*, *303*, 79–91.

White, W., Schilling, J.-G., & Hart, S. (1976). Evidence for the Azores mantle plume from strontium isotope geochemistry of the Central North Atlantic. *Nature*, *263*, 659.

Wieser, M. E., Buhl, D., Bouman, C., & Schwieters, J. (2004). High precision calcium isotope ratio measurements using a magnetic sector multiple collector inductively coupled plasma mass spectrometer. *Journal of Analytical Atomic Spectrometry*, *19*, 844–851.

Wimpenny, J., Colla, C. A., Yin, Q.-Z., Rustad, J. R., & Casey, W. H. (2014). Investigating the behaviour of Mg isotopes during the formation of clay minerals. *Geochimica et Cosmochimica Acta*, *128*, 178–194.

Wolfram Research, I. (2018) Mathematica, 11.3 ed. Wolfram Research, Inc., Champaign, Illinois.

Wombacher, F., Eisenhauer, A., Heuser, A., & Weyer, S. (2009). Separation of Mg, Ca and Fe from geological reference materials for stable isotope ratio analyses by MC-ICP-MS and double-spike TIMS. *Journal of Analytical Atomic Spectrometry*, *24*, 627–636.